

1 **Measurements of the Net Charge Density of Space Plasmas**

2
3 Chao Shen^{1*}, Yufei Zhou¹, and Lai Gao¹

4 ¹School of Science, Harbin Institute of Technology, Shenzhen, 518055, China

5
6 Corresponding author: Chao Shen (shenchao@hit.edu.cn)

7 8 **Key Points:**

9 Charge densities in space have been calculated using MMS electric field measurements
10 for the first time.

11
12 A method for extracting the charge density from 10-point electric potential
13 measurements is presented.

14
15 An additional scheme to measure the charge density using seven or eight electric
16 potential probes is explored.

17 18 19 **Key Words:**

20 Charge Density, Electric Field, Electric Potential Measurements, Multi-Point
21 Measurements, Magnetopause

22

23 **Abstract**

24 Space plasmas are composed of charged particles that play a key role in electromagnetic
25 dynamics. However, to date, there has been no direct measurement of the distribution
26 of such charges in space. In this study, three schemes for measuring charge densities in
27 space are proposed. The first scheme is based on electric field measurements by
28 multiple spacecraft. This method is applied to deduce the charge density distribution
29 within Earth's magnetopause boundary layer using Magnetospheric MultiScale
30 constellation (MMS) 4-point measurements, and indicates the existence of a charge
31 separation there. The second and third schemes proposed are both based on electric
32 potential measurements from multiple electric probes. The second scheme, which
33 requires 10 or more electric potential probes, can yield the net charge density to first-
34 order accuracy, while the third scheme, which makes use of seven to eight specifically
35 distributed probes, can give the net charge density with second-order accuracy. The
36 feasibility, reliability, and accuracy of these three schemes are successfully verified for
37 a charged-ball model. These charge density measurement schemes could potentially be
38 applied in both space exploration and ground-based laboratory experiments.

39

40

41

42

43

44

45 **1. Introduction**

46

47 Electromagnetic fields are omnipresent in space. They control the motion of
48 plasmas, and the transportation, release, and transformation of energy in space, and
49 thereby are the key driver of space weather hazards. Charges and electric currents
50 (flows of charged particles) source the electromagnetic field, and therefore the
51 distribution and motions of charges determine its form. Charge separations occur in
52 electric double layers, which exist commonly in space plasmas (Block, 1975; Akasofu,
53 1981; Raadu, 1989). Net charges can appear in plasma boundary layers (Parks, 1991),
54 e.g., the magnetopause boundary layers and Alfvén layers (Hasegawa and Sato, 1989).
55 Charge separations can also occur during ambipolar diffusion processes (Alfvén, 1963;
56 Bittencourt, 2004), e.g., the Earth's polar wind (Axford, 1968; Lemaire and Pierrard,
57 2001; Yau et al., 2007). In macro-scale plasmas, flow shears or vorticities can
58 accumulate these net charges, driving the field-aligned currents (Michael, 2014).
59 Charge separations also play a key role in plasma instabilities, e.g., the Rayleigh-Taylor
60 instability (Treumann and Baumjohann, 1997; Michael, 2014) and the tearing
61 instability (Treumann and Baumjohann, 1997).

62 The acquisition of a spatial distribution of electric charge density is of critical
63 importance for recognizing and understanding the dynamics of electromagnetic fields
64 and plasmas in space. However, there is still no equipment available for directly
65 measuring the net charge density in space, although measurements of the charge density

66 in the atmosphere near the ground have been achieved. The difficulty of such
67 measurements in space arises because the plasmas there are extremely thin, with only
68 a few charged particles per cm^3 , and the net charge density is even lower by several
69 orders. This article investigates how the charge density can be measured using 4-point
70 electric field measurements from the Magnetospheric MultiScale (MMS) constellation
71 (Burch et al., 2016) and also explores how the charge density can be deduced based on
72 multiple-probe electric potential measurements on board a single spacecraft.

73 In Section 2, we discuss a method for deducing the charge density from 4-point
74 electric field measurements, which has been applied to analyze the charge density
75 distribution in the dayside magnetopause boundary layer during an MMS
76 magnetopause crossing event. In Section 3, a method for deducing the charge density
77 from ≥ 10 -point electric potential measurements is studied. Section 4 explores
78 measurements of the charge density based on seven or eight electric potential probes.
79 Section 5 gives a summary and some discussion.

80

81 **2. Deducing the charge density from multi-spacecraft electric field measurements**

82 The direct approach to obtain the net charge density is to sum up the charge
83 densities of positively and negatively charged particles with the formula

$$84 \quad \rho = -en_e + \sum_i q_i n_i, \quad (1)$$

85 where n_e and n_i are the densities of the electrons and the i -th ion, respectively, and
86 q_i is the charge of the i -th ion. However, the electric force is so strong that the plasmas
87 are always quasi-neutral, and the separation between the two types of charges is very

88 slight. Therefore, the charge densities in space plasmas are extremely small. It is almost
 89 impossible to determine the net charge density by measuring the densities of charged
 90 particles at the present stage of space exploration.

91 The most feasible and practicable method at present is to deduce the net charge
 92 density by measuring the electric potentials or electric fields created by the net charges
 93 at high accuracies with well-developed technology (Mozer et al., 1967; Mozer, 1973;
 94 Paschmann et al., 1997; Pedersen et al., 1998; Michael, 2014). The Spin-plane Double
 95 Probes (SDPs) and Axial Double Probes (ADPs) (Torbert et al., 2016; Lindqvist et al.,
 96 2016; Ergun et al., 2016) onboard the four spacecraft of the MMS constellation (Burch
 97 et al., 2016) yield four electric field vectors at four different locations separated by tens
 98 of kilometers. With the Gaussian theorem, $\rho = \epsilon_0 \nabla \cdot \mathbf{E}$, we can get the charge density at
 99 the center of the constellation, as illustrated in Fig. 1. Suppose that the four spacecraft
 100 of the MMS constellation are located at four different positions \mathbf{r}_α ($\alpha = 1, 2, \dots, 4$). The
 101 barycenter of the MMS constellation is $\mathbf{r}_c \equiv \frac{1}{4} \sum_{\alpha=1}^4 \mathbf{r}_\alpha$. It is convenient to assume that
 102 $\mathbf{r}_c = 0$, so that the barycenter of the constellation is the origin of the frame of reference.
 103 The four spacecraft yield four electric fields, $\mathbf{E}_\alpha = \mathbf{E}(\mathbf{r}_\alpha)$, $\alpha = 1, 2, \dots, 4$. The i -th component
 104 of the gradient of the electric field at the barycenter can be calculated as (Harvey, 1998;
 105 Chanteur, 1998)

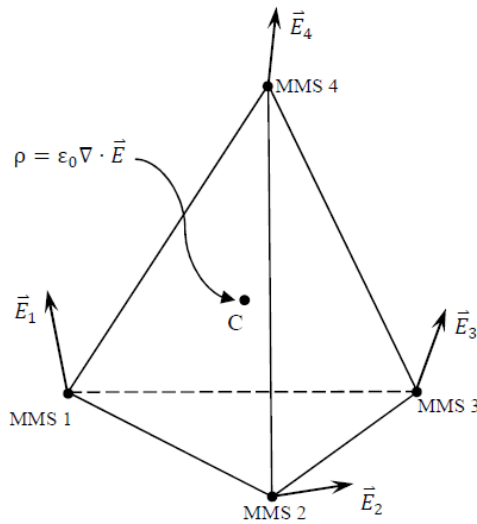
$$106 \quad (\nabla_i \mathbf{E})_c = \frac{1}{4} \sum_{\alpha=1}^4 \mathbf{E}_\alpha r_{\alpha j} \mathbf{R}_{ji}^{-1}, \quad (2)$$

107 where $\mathbf{R}_{ij} = \frac{1}{4} \sum_{\alpha=1}^4 r_{\alpha i} r_{\alpha j}$ is the volumetric tensor of the constellation (Harvey, 1998), and
 108 \mathbf{R}_{ji}^{-1} its inverse. By using the Gaussian theorem, we can get the charge density with the

109 divergence of the electric field vector, i.e.,

110
$$\rho = \epsilon_0 \nabla \cdot \mathbf{E} = \epsilon_0 \sum_{i=1}^3 \nabla_i E_i, \quad (3)$$

111



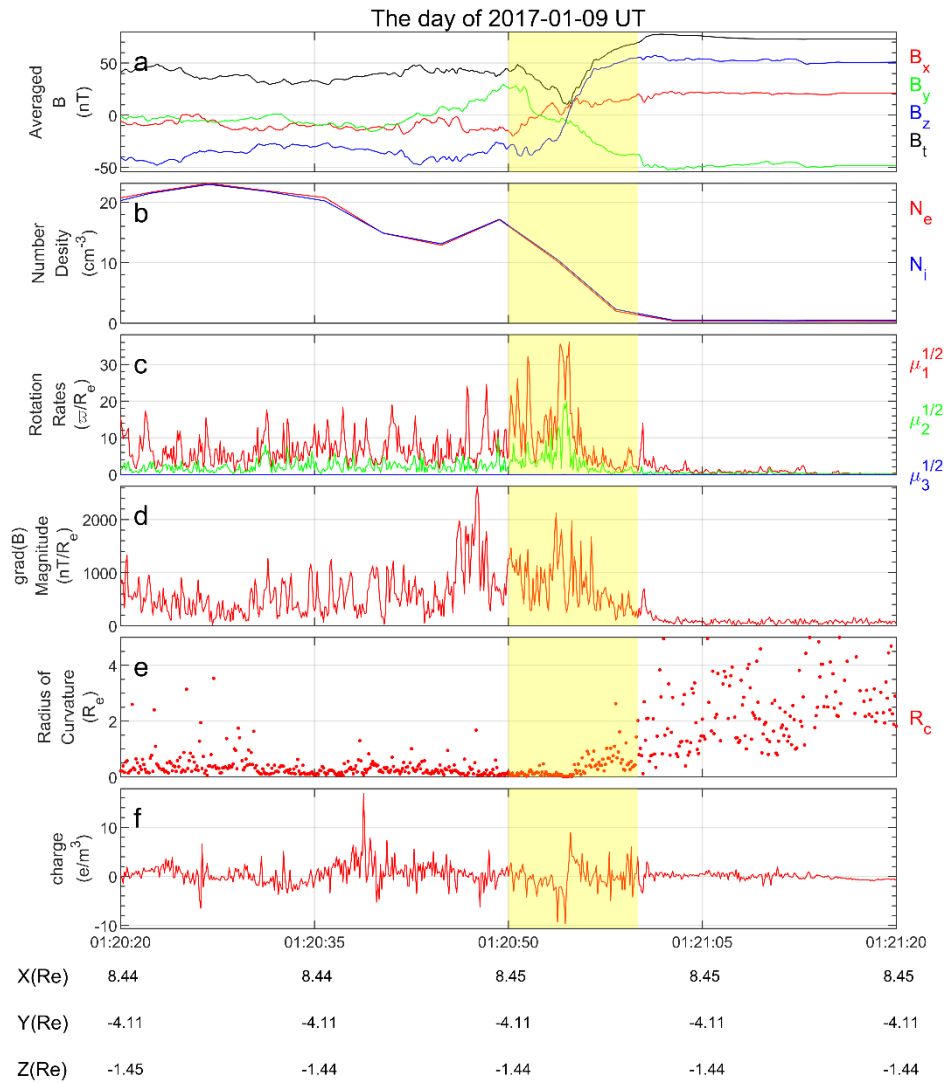
112

113 **Figure 1.** A schematic view of the measurements of the electric field by the MMS
114 constellation and the calculation of the charge density.

115

116 Here we will explore the net charge distribution within the magnetopause
117 boundary layer based on MMS electric measurements. It is well known that a charge
118 separation occurs in the magnetopause, brought about by the effects of inertia (because
119 there is a large difference between the masses of the electrons and ions). As a result of
120 that, the net positive charges accumulate at the magnetospheric side and the net negative
121 charges accumulate at the magnetosheath side of the magnetopause boundary. Because
122 the MMS constellation has a rather small size (with the spacecraft separations being
123 several tens of kilometers) and can be well-embedded in the magnetopause boundary,

124 the charge density can be deduced from the MMS electric observations using the above
125 method. We investigate one MMS magnetopause crossing event at 1:20:50 on 9 January
126 2017 by examining the electric field and calculating the charge density, whose values
127 during the crossing event are shown in Fig. 2. It can be seen that the rotational
128 discontinuity (RD) appear at UT01:20:55 with the maximum magnetic rotation rates
129 (Panel (c)) (Shen et al., 2007), minimum value of the gradient of the magnetic strength
130 (Panel (d)), and smallest radius of curvature of the magnetic field lines (Panel (e)). As
131 shown in Panel (f), a charge separation is evident at the two sides of the rotational
132 discontinuity (RD), with the positive charges at the magnetospheric side and negative
133 charges at the magnetosheath side. The maximum value of the charge density in the
134 magnetopause is about $10 e / m^3$. It is evident that the electric neutrality is kept in the
135 magnetosphere near to the magnetopause. These results are in agreement with the
136 conventional models of the magnetopause boundary layers (Parks, 1991; Kivelson and
137 Russell, 1995).



138

139 **Figure 2.** The structure of the magnetopause during an MMS crossing event on 9

140 January 2017. From top to bottom: (a) the magnetic flux density at the center of the

141 constellation, (b) the electron and ion number densities measured by MMS-1 (Pollock

142 et al., 2016), (c) the rotation rates of the magnetic field (Shen et al., 2007), (d) $|\nabla|\mathbf{B}||$,

143 (e) the radius of curvature of the magnetic field lines (Shen et al., 2003), and (f) the

144 charge distribution. The yellow shading indicates the rotational discontinuity (RD)

145 crossing.

146

147 **3. Charge density measurements from 10 probes on board a spacecraft – Stiff**

148 **Booms Method**

149

150 It is known that the linear gradient of a quantity can be estimated based on 4-point
151 measurements (Harvey, 1998; Chanteur, 1998; Shen et al., 2003), while the quadratic
152 gradient of a quantity can be calculated based on 10-point measurements (Chanteur,
153 1998). In a previous investigation (Shen et al., 2021), a new algorithm was put forward
154 to calculate the linear and quadratic gradients jointly based on 10 or more measurements.
155 It can be applied to obtain the quadratic gradients ($\nabla^2\varphi$) from 10-point electric
156 potential field (φ) measurements. Moreover, with the Poisson equation,

157
$$\rho = -\varepsilon_0 \nabla^2 \varphi, \quad (4)$$

158 it yields the distribution of the electric charge density.

159

160 The electric field generated by a uniformly-charged ball will be used to test this
161 approach. Supposing that the radius of the ball is r_0 and its charge density is ρ , we
162 get the electric potential field analytically as,

163
$$\varphi(\mathbf{r}) = \begin{cases} -\frac{1}{6}\varepsilon^{-1}\rho r^2 + \frac{1}{2\varepsilon}r_0^2\rho & \text{if } r \leq r_0, \\ -\frac{1}{4\pi\varepsilon}\frac{Q}{r} & \text{if } r \geq r_0, \end{cases} \quad (5)$$

164 where $Q = \frac{4}{3}\pi r_0^3\rho$ is the total charge and r is the distance from the center of the ball
165 to the measurement point. In the following modeling, constant values of 1 are assigned
166 to ρ , r_0 , and ε . The positions of the 10 probes in the barycenter coordinates are
167 generated randomly and presented in Tab. 1 and Fig. 3. The three characteristic lengths
168 of the distribution of the 10 probes (Harvey, 1998; Robert, et al., 1998) are $a = 0.10$,

169 $b = 0.06$, and $c = 0.03$. The reconstructed characteristic matrix \mathfrak{R}^{MN} is

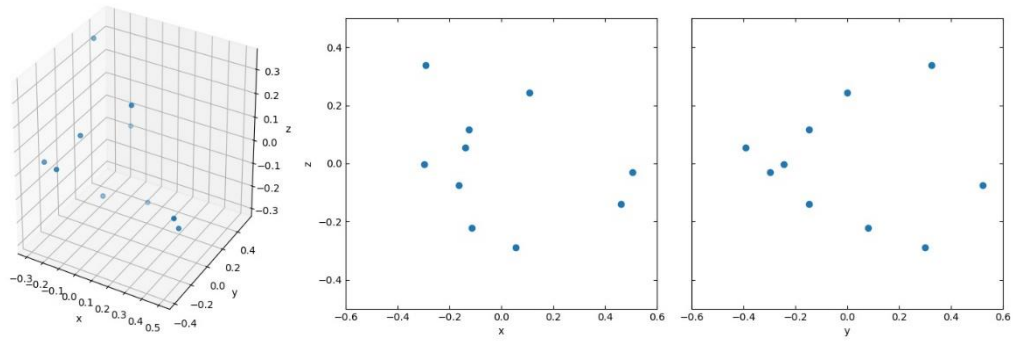
$$170 \quad (\mathfrak{R}^{MN}) = \begin{pmatrix} 12.73 & -11.09 & -5.05 & 5.22 & 2.74 & 1.61 \\ -11.09 & 20.90 & 5.47 & -6.71 & -4.97 & -2.28 \\ -5.05 & 5.47 & 6.44 & -2.49 & -4.56 & -2.27 \\ 5.22 & -6.71 & -2.49 & 12.83 & -1.91 & 2.27 \\ 2.74 & -4.97 & -4.56 & -1.91 & 9.09 & 0.86 \\ 1.61 & -2.28 & -2.27 & 2.27 & 0.86 & 2.68 \end{pmatrix} 10^{-3}, \quad (6)$$

171 and its eigenvalues are given in Tab. 2.

172

173 **Table 1.** The distribution of the 10 spacecraft of the constellation.

x	y	z
-0.16474	0.520923	-0.07516
-0.29774	-0.2433	-0.00151
0.107263	-0.00029	0.243785
-0.12458	-0.14707	0.116693
-0.11324	0.080113	-0.22108
0.505285	-0.29726	-0.0293
0.055479	0.300437	-0.28976
0.461577	-0.14647	-0.13865
-0.2916	0.323618	0.339179
-0.13771	-0.3907	0.055801



174

175

Figure 3. The distribution of the 10 probes.

176

177

Table 2. The eigenvalues of the characteristic matrix \mathfrak{R}^{MN} .

0.03614	0.01326	0.00114	0.00235	0.00510	0.00668
---------	---------	---------	---------	---------	---------

178

179

We first investigate the behavior of the resultants with the number of iterations.

180

D is the local characteristic scale of the electric field structure and is set equal to r in

181

this model. It is assumed that the barycenter of the constellation is at $[0.1,0,0]$, and the

182

probe separations L are reduced proportionally so that the relative measurement scale

183

$L/D= 0.026$. The relative truncation error, $X_{algorithm}/X_{real} - 1$, is shown in Fig. 4.

184

With increasing numbers of iterations, the errors decrease and finally converge to

185

certain fixed values. In this calculation, the solution converges after 100 iterations. By

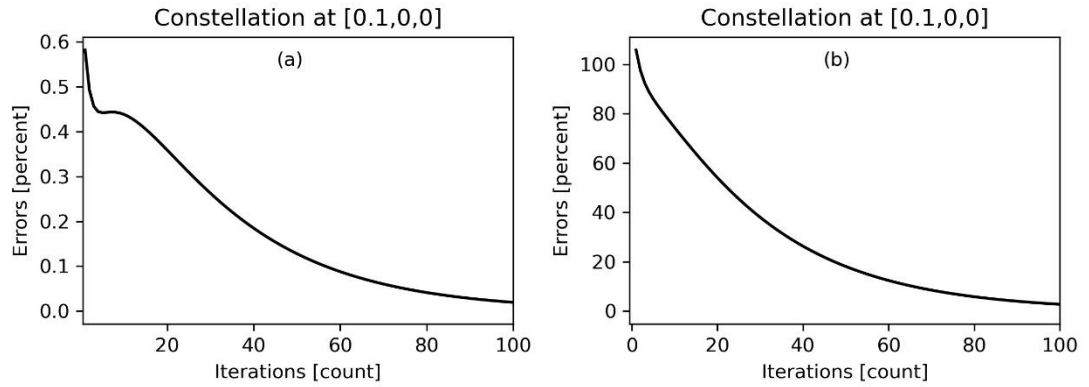
186

testing various fields, we found that the number of iterations required for convergence

187

varies.

188



189

190 **Figure 4.** The relative errors of the linear (a) and the quadratic (b) electric potential
 191 gradients, i.e., $\partial_x \phi$ and $\partial_x \partial_x \phi$, calculated for different numbers of iterations at
 192 $[0.1,0,0]$ within the charged ball.

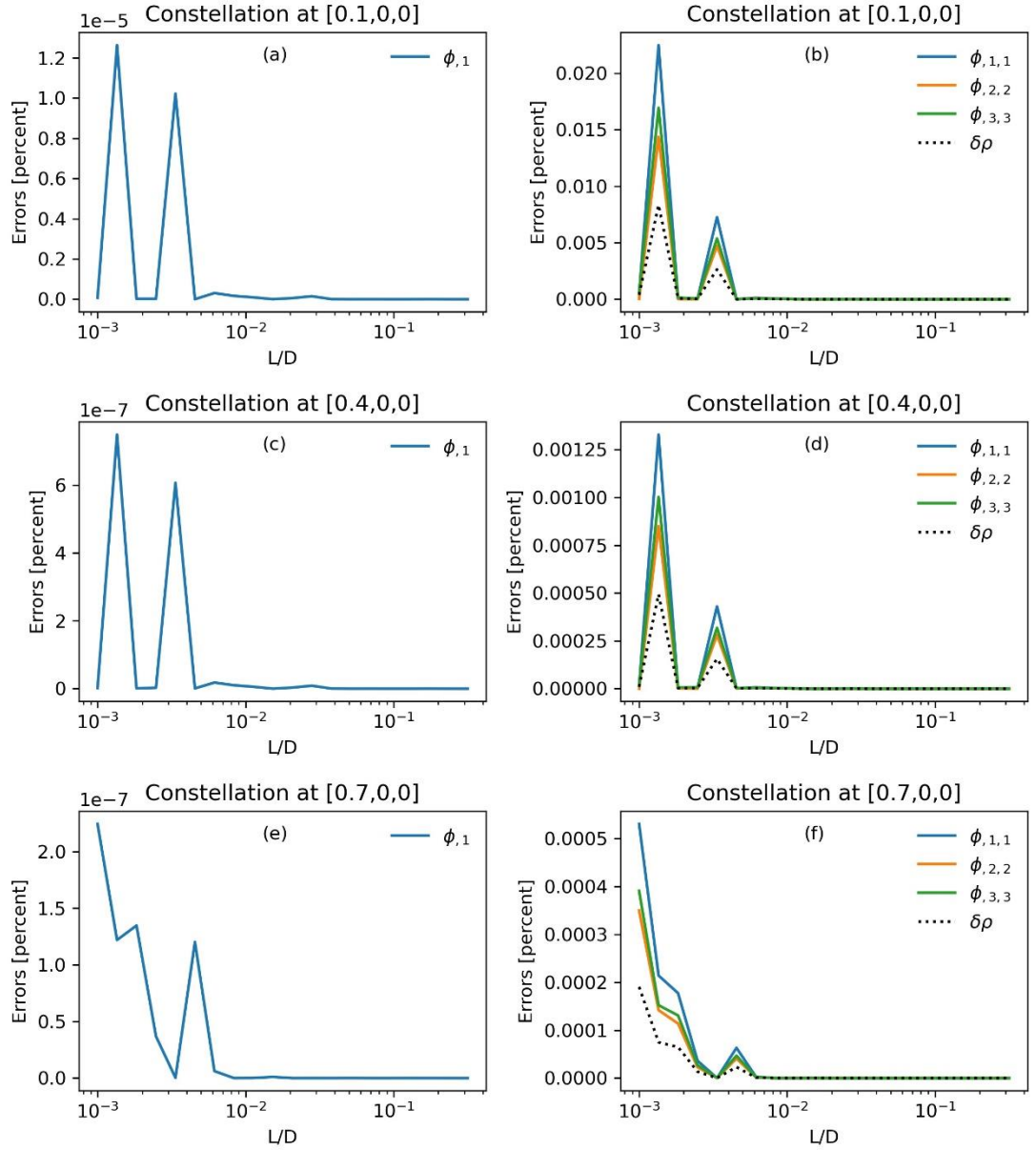
193

194 Secondly, we investigate the dependence of the truncation errors on the relative
 195 measurement scale L/D . We have tested six situations, with the barycenter of the 10
 196 probes located at three representative points within the ball, $[0.1,0,0]$, $[0.4,0,0]$, and
 197 $[0.7,0,0]$, and three points outside the ball, $[3,0,0]$, $[5,0,0]$, and $[8,0,0]$. We scale up
 198 and down the size of the original 10 probes to adjust the characteristic size L and
 199 therefore L/D .

200

201 Figure 5 shows the truncation errors modeled in the ball. In general, the errors
 202 are less than $10^{-5}\%$ for the linear gradients and less than 0.02% for the quadratic
 203 gradients. With the same number of iterations, 1000, the errors at different positions
 204 vary by an order of 2.

205



206

207 **Figure 5.** The left panels, (a), (b), and (c), show the truncation errors for the non-

208 vanishing component of the linear gradient by L/D calculated for three different

209 locations of the barycenter of the 10 probes inside the ball, $[0.1,0,0]$, $[0.4,0,0]$, and

210 $[0.7,0,0]$. The right panels, (b), (d), and (f), illustrate the relative errors of the non-

211 vanishing components of the quadratic gradient and charge density (dashed line)

212 calculated for the same three locations of the barycenter. It is noted that $\phi_{,1} \equiv \partial_x \phi$

213 and $\phi_{,2,2} \equiv \partial_y \partial_y \phi$, where a comma denotes partial differentiation.

214

215

Figure 6 shows the modeling results outside of the ball. As $L/D < 0.01$, the

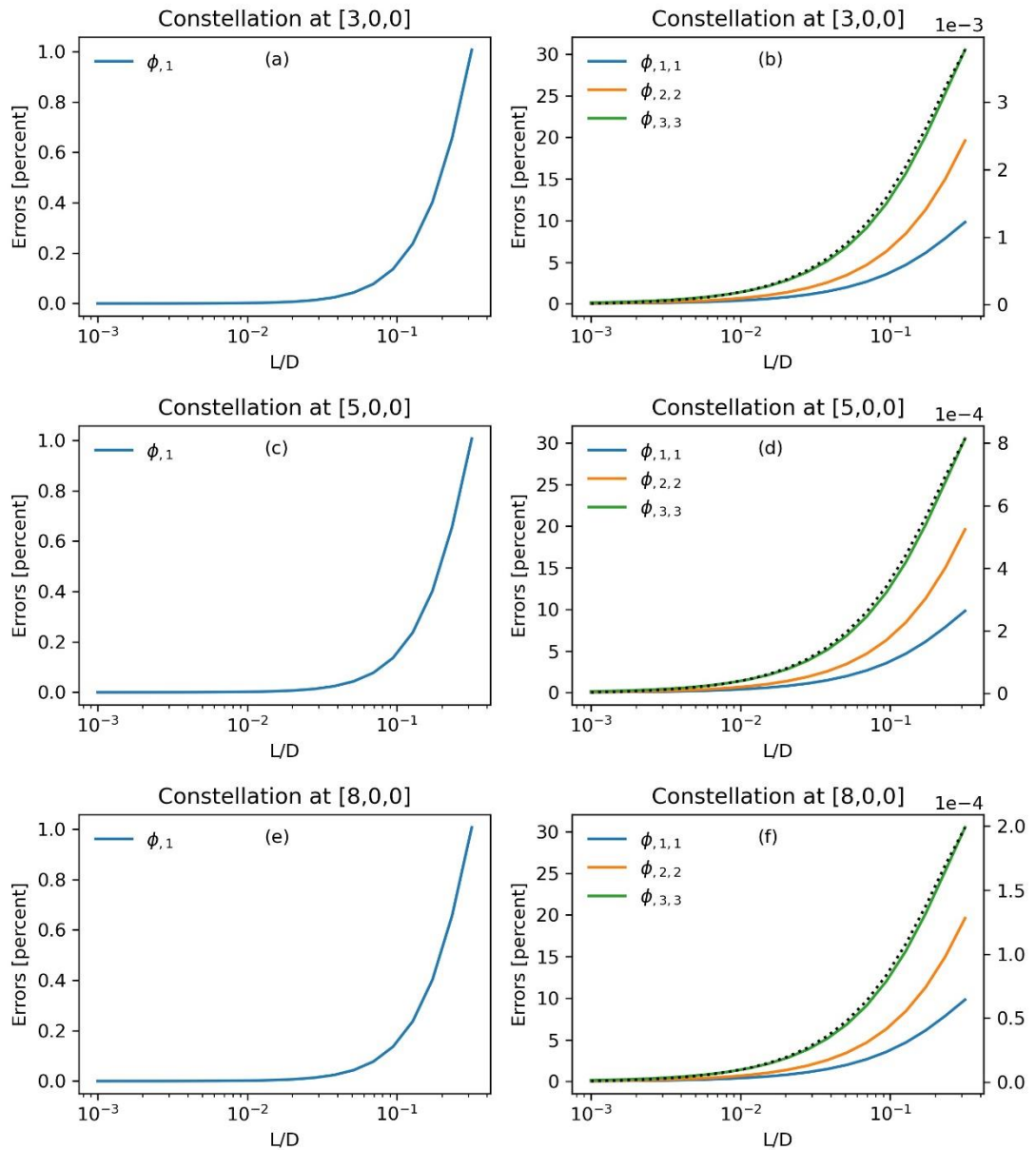
216

relative errors of the non-vanishing quadratic gradient components are below 2%. The

217

attained linear and quadratic gradients accurate to second order.

218



219

220

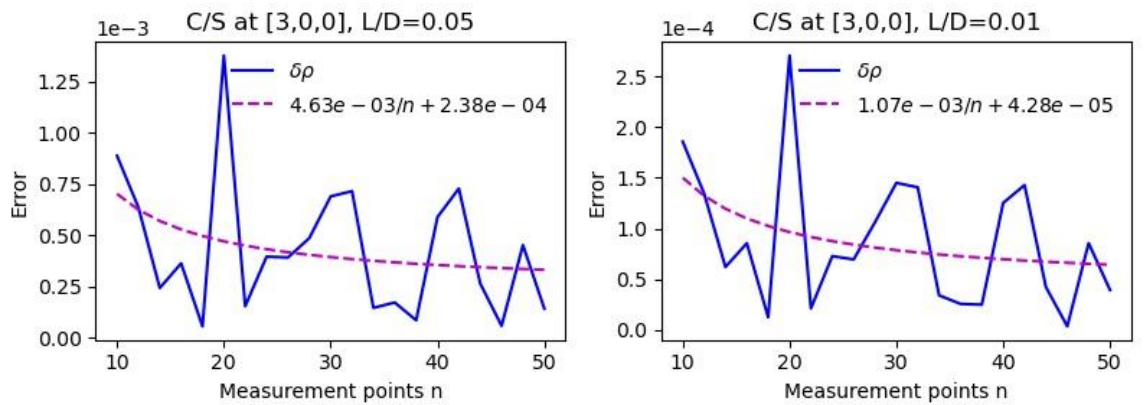
Figure 6. The left panels, (a), (b), and (c), show the truncation error for the non-

221

vanishing component of the linear gradient as a function of L/D calculated for three

222 different locations of the barycenter of the 10 probes outside of the ball, [3,0,0],
 223 [5,0,0], and [8,0,0]. The right panels, (b), (d), and (f), illustrate the relative errors of
 224 the non-vanishing components of the quadratic gradient and the absolute value of the
 225 charge density (dashed line) calculated for the same three locations of the barycenter. It
 226 is noted that the real charge density outside of the ball is zero.

227



228

229 **Figure 7.** The relation between the absolute error of the charge density and the number
 230 of measurement points at [3,0,0]. The relative measurement scale is chosen as $L/D =$
 231 0.05 (left) and $L/D = 0.01$ (right). The dashed lines are fitted from the modeled
 232 errors.

233

234 We further investigate the relationship between the accuracy of the density
 235 estimated and the number of the probes used. Figure 7 indicates that the accuracy of the
 236 charge density is not improved significantly as the number of probes is increased.
 237 Therefore, 10 probes with a proper spatial configuration will be sufficient for robust
 238 measurements of the charge density.

239 This scheme is possible to be used for the net charge measurements on the low

240 Earth orbits at the altitudes of several hundred kms, for which the 10 probes are
241 mounted at the ends of 10 booms with different lengths, and the spacecraft can be either
242 spinning or not.

243

244 **4. Measuring the charge density with seven or eight electric potential probes**

245 Only three diagonal components of the quadratic gradient of the electric potential
246 are contained in the Poisson equation ($\rho \propto \nabla^2\phi = \frac{\partial^2}{\partial x^2}\phi + \frac{\partial^2}{\partial y^2}\phi + \frac{\partial^2}{\partial z^2}\phi$). The
247 three other cross-components of the quadratic gradient, $\partial_x\partial_y\phi$, $\partial_y\partial_z\phi$, and $\partial_z\partial_x\phi$,
248 are of no use for computing the charge density, so three independent parameters can be
249 neglected in this algorithm. Therefore, $10-3=7$ probes are sufficient to acquire the data
250 for the estimation of the Laplacian operator on the electric potential ($\nabla^2\phi$) as well as
251 the charge density.

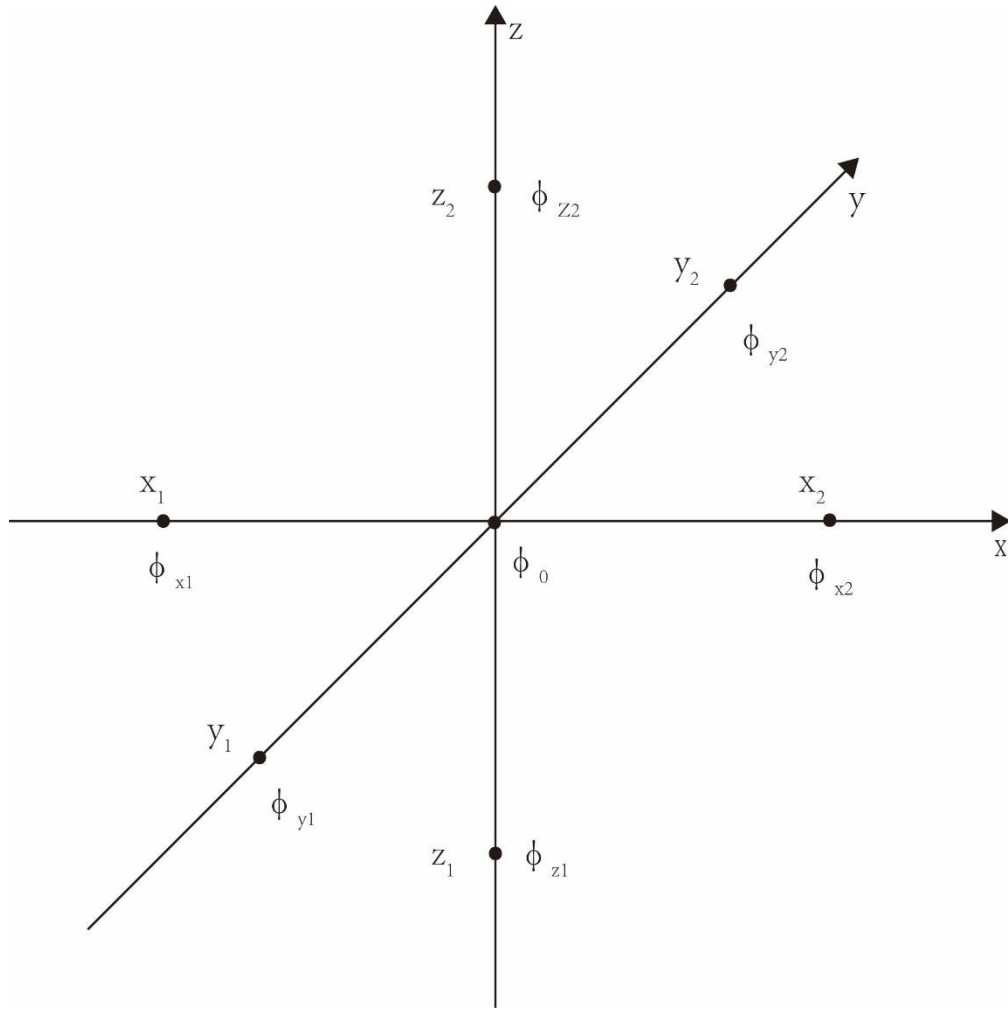
252

253 **4.1 Seven-probe scheme**

254 A seven-probe scheme, which is similar to the electric potential measurement of
255 the MMS at high altitude orbits, is shown in Fig. 8. All probes are placed on three axes
256 of the Cartesian coordinate system. The spatial parameters are $x_2 = -x_1 = L_x$,
257 $y_2 = -y_1 = L_y$, and $z_2 = -z_1 = L_z$. By taking differences, the linear and quadratic
258 gradients at second-order accuracy can be obtained to estimate the charge density at the
259 center.

260

261



262

263 **Figure 8.** A schematic view of the seven-probe measurement of the charge density. The
 264 probes are indicated by black dots.

265

266 The linear and quadratic gradients along the x-axis are

$$\left\{ \begin{array}{l} \partial_x \phi = \frac{\phi_{x2} - \phi_{x1}}{2L_x} \quad (7) \\ \partial_x^2 \phi = -\frac{\frac{\phi_{x2} - \phi_0}{L_x} - \frac{\phi_0 - \phi_{x1}}{L_x}}{L_x} = \frac{(\phi_{x2} + \phi_{x1}) - 2\phi_0}{L_x^2} \quad (8) \end{array} \right.$$

268 Similarly, the linear and quadratic gradients along the y-axis are

$$\left\{ \begin{array}{l} \partial_y \phi = \frac{\phi_{y2} - \phi_{y1}}{2L_y} \quad (9) \\ \partial_y^2 \phi = \frac{(\phi_{y2} + \phi_{y1}) - 2\phi_0}{L_y^2} \quad (10) \end{array} \right.$$

The linear and quadratic gradients along the z-axis are

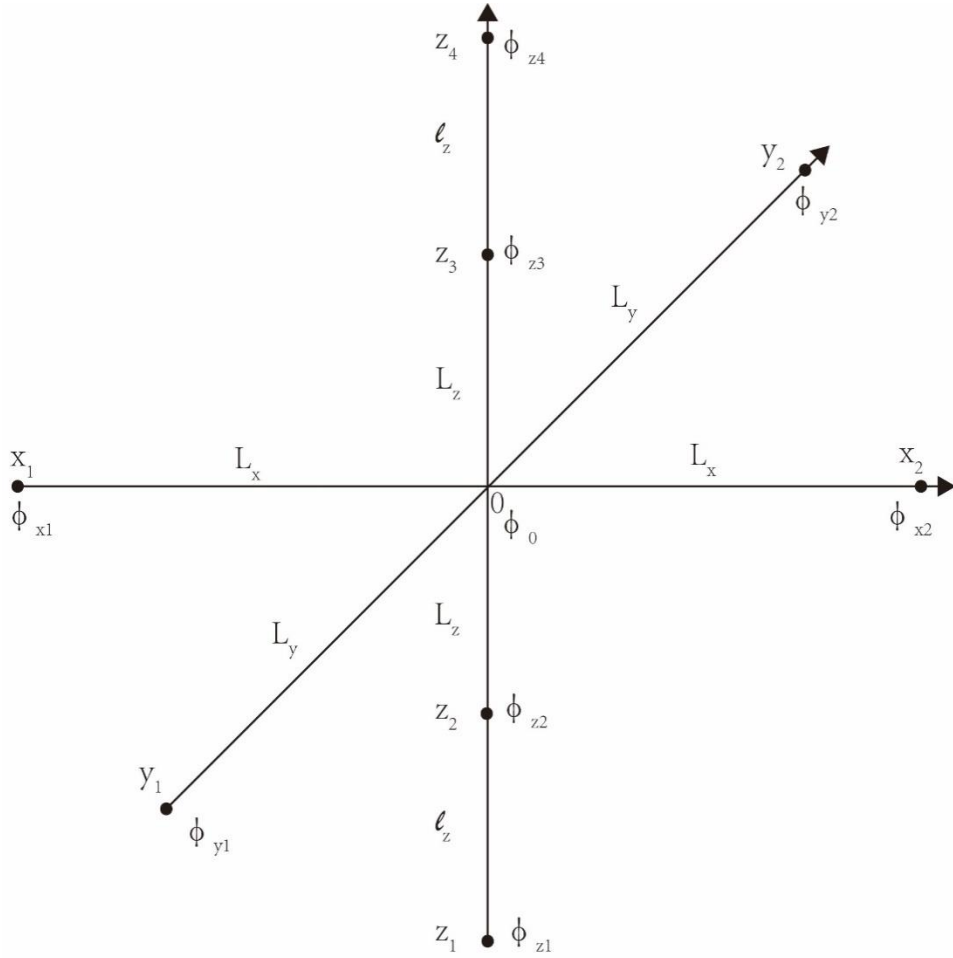
$$\left\{ \begin{array}{l} \partial_z \phi = \frac{\phi_{z2} - \phi_{z1}}{2L_z} \quad (11) \\ \partial_z^2 \phi = \frac{(\phi_{z2} + \phi_{z1}) - 2\phi_0}{L_z^2} \quad (12) \end{array} \right.$$

The linear and quadratic gradients are both accurate to second order.

However, in actual measurements, the central probe is inside the spacecraft and cannot determine the electric potential accurately. To improve this measurement, the central probe is replaced by another two additional probes located on the z-axis. The algorithm for this is shown in the following section. It is noted the seven-probe scheme can be still applied to the electric field and charge density measurements in ground-based laboratory experiments.

4.2 Eight-probe scheme

The eight-probe scheme is shown in Fig. 9 with $x_2 = -x_1 = L_x$, $y_2 = -y_1 = L_y$, $z_3 = -z_2 = L_z$, and $z_4 = -z_1 = L_z + l_z$. The algorithm is constructed as follows.



284

285 **Figure 9.** A schematic view of the eight-probe measurement of charge density.

286

287

288 The four electric potentials observed by the probes on the z-axis can be expressed as a

289 Taylor series. By keeping the first five terms we get

290

$$\left\{ \begin{array}{l} \phi_{z1} = \phi_0 + z_1 \partial_z \phi + \frac{1}{2} z_1^2 \partial_z^2 \phi + \frac{1}{3!} z_1^3 \partial_z^3 \phi + \frac{1}{4!} z_1^4 \partial_z^4 \phi \end{array} \right. \quad (13)$$

$$\left\{ \begin{array}{l} \phi_{z2} = \phi_0 + z_2 \partial_z \phi + \frac{1}{2} z_2^2 \partial_z^2 \phi + \frac{1}{3!} z_2^3 \partial_z^3 \phi + \frac{1}{4!} z_2^4 \partial_z^4 \phi \end{array} \right. \quad (14)$$

$$\left\{ \begin{array}{l} \phi_{z3} = \phi_0 + z_3 \partial_z \phi + \frac{1}{2} z_3^2 \partial_z^2 \phi + \frac{1}{3!} z_3^3 \partial_z^3 \phi + \frac{1}{4!} z_3^4 \partial_z^4 \phi \end{array} \right. \quad (15)$$

$$\left\{ \begin{array}{l} \phi_{z4} = \phi_0 + z_4 \partial_z \phi + \frac{1}{2} z_4^2 \partial_z^2 \phi + \frac{1}{3!} z_4^3 \partial_z^3 \phi + \frac{1}{4!} z_4^4 \partial_z^4 \phi \end{array} \right. \quad (16)$$

291

292 Summing up the above four equations leads to

$$293 \quad (\phi_{z1} + \phi_{z2} + \phi_{z3} + \phi_{z4}) = 4\phi_0 + \frac{1}{2}(z_1^2 + z_2^2 + z_3^2 + z_4^2)\partial_z^2\phi + \frac{1}{4!}(z_1^4 + z_2^4 + z_3^4 + z_4^4)\partial_z^4\phi .$$

294 The electric potential at the center is therefore

$$295 \quad \phi_0 = \frac{1}{4}(\phi_{z1} + \phi_{z2} + \phi_{z3} + \phi_{z4}) - \frac{1}{8}(z_1^2 + z_2^2 + z_3^2 + z_4^2)\partial_z^2\phi - \frac{1}{96}(z_1^4 + z_2^4 + z_3^4 + z_4^4)\partial_z^4\phi \quad (17)$$

296 Subtracting Eq. (13) from Eq. (16) and Eq. (14) from Eq. (15) gives

$$297 \quad \begin{cases} \phi_{z4} - \phi_{z1} = (z_4 - z_1) \partial_z\phi + \frac{1}{3!}(z_4^3 - z_1^3)\partial_z^3\phi \\ \phi_{z3} - \phi_{z2} = (z_3 - z_2) \partial_z\phi + \frac{1}{3!}(z_3^3 - z_2^3)\partial_z^3\phi \end{cases} \quad (18)$$

298 or

$$299 \quad \begin{cases} \phi_{z4} - \phi_{z1} = 2z_4\partial_z\phi + \frac{1}{3}z_4^3\partial_z^3\phi \\ \phi_{z3} - \phi_{z2} = 2z_3\partial_z\phi + \frac{1}{3}z_3^3\partial_z^3\phi \end{cases} \quad (18')$$

300 Then, we get the linear gradient along the z-axis at the center as

$$301 \quad \partial_z\phi = \frac{z_3^3(\phi_{z4} - \phi_{z1}) - z_4^3(\phi_{z3} - \phi_{z2})}{2z_4z_3^3 - 2z_3z_4^3} \quad (19)$$

302 The expression above is of fourth-order accuracy. On the other hand, from Equation

303 (18), the third-order derivative of electric potential along the z-axis is

$$304 \quad \partial_z^3\phi = \frac{3z_3(\phi_{z4} - \phi_{z1}) - 3z_4(\phi_{z3} - \phi_{z2})}{z_3z_4^3 - z_4z_3^3} \quad (20)$$

305 The expression above is of second-order accuracy.

306 Subtracting the sum of Eq. (14) and Eq. (15) from the sum of Eq. (13) and Eq. (16), we

307 get

308 $(\phi_{z4} + \phi_{z1}) - (\phi_{z3} + \phi_{z2}) = \frac{1}{2}(z_1^2 + z_4^2 - z_2^2 - z_3^2)\partial_z^2\phi + \frac{1}{4!}(z_1^4 + z_4^4 - z_2^4 - z_3^4)\partial_z^4\phi$

309 The second-order derivative is, therefore,

310
$$\partial_z^2\phi = \frac{2(\phi_{z4} + \phi_{z1} - \phi_{z3} - \phi_{z2})}{(z_1^2 + z_4^2 - z_2^2 - z_3^2)} - \frac{1}{12} \frac{(z_1^4 + z_4^4 - z_2^4 - z_3^4)}{z_1^2 + z_4^2 - z_2^2 - z_3^2} \partial_z^4\phi \quad (21)$$

311 The expression above is of second-order accuracy.

312 Substituting Eq. (21) into Eq. (17), we get the corrected potential ϕ_0 at the center
313 as

314
$$\phi_0 = \frac{1}{4}(\phi_{z1} + \phi_{z2} + \phi_{z3} + \phi_{z4}) - \frac{1}{4} \frac{z_1^2 + z_2^2}{z_1^2 - z_2^2} (\phi_{z4} + \phi_{z1} - \phi_{z3} - \phi_{z2}) + \frac{1}{24} z_1^2 z_2^2 \partial_z^4\phi \quad (17')$$

315 The above expression is of fourth-order accuracy because the expression is
316 truncated at the fourth-order term.

317 Furthermore, by neglecting high order terms, we get the estimators for the
318 potential and its linear and quadratic gradients at the center as

$$\left\{ \begin{array}{l} \partial_z^2\phi = \frac{(\phi_{z4} + \phi_{z1}) - (\phi_{z3} + \phi_{z2})}{l_z(2L_z + l_z)} \quad (21') \\ \partial_z\phi = \frac{(L_z + l_z)^3(\phi_{z3} - \phi_{z2}) - L_z^3(\phi_{z4} - \phi_{z1})}{2L_z(L_z + l_z)(2l_zL_z + l_z^2)} \quad (19') \\ \phi_0 = \frac{1}{4}(\phi_{z1} + \phi_{z2} + \phi_{z3} + \phi_{z4}) - \frac{(L_z + l_z)^2 + L_z^2}{4l_z(2L_z + l_z)} (\phi_{z4} + \phi_{z1} - \phi_{z3} - \phi_{z2}) \quad (17'') \end{array} \right.$$

320 As stated above, the second-order derivative along the z-axis is of second-order
321 accuracy. The potential and its first-order derivative along the z-axis are of fourth-order
322 accuracy.

323 Similar to the seven-probe scheme, the first-order and second-order derivatives of
324 the potential along the x- and y-axis are subjected to Eqs. (7)-(10). The central potential

325 ϕ_0 is calculated with Eq. (17''). The first-order and second-order derivatives along the
 326 x- and y-axis are of second order accuracy.

327 The electric field at the center is

$$328 \quad \mathbf{E} = -\hat{\mathbf{e}}_x \partial_x \phi - \hat{\mathbf{e}}_y \partial_y \phi - \hat{\mathbf{e}}_z \partial_z \phi \quad (22)$$

329 Using the Poisson equation (4), the charge density is obtained as

$$330 \quad \begin{aligned} \rho &= -\varepsilon_0 (\partial_x^2 \phi + \partial_y^2 \phi + \partial_z^2 \phi) \\ &= -\varepsilon_0 \left[\frac{(\phi_{x2} + \phi_{x1}) - 2\phi_0}{L_x^2} + \frac{(\phi_{y2} + \phi_{y1}) - 2\phi_0}{L_y^2} + \frac{(\phi_{z4} + \phi_{z1}) - (\phi_{z3} + \phi_{z2})}{l_z(2L_z + l_z)} \right] \end{aligned} \quad (23)$$

331 where ϕ_0 is given by Eq. (17'').

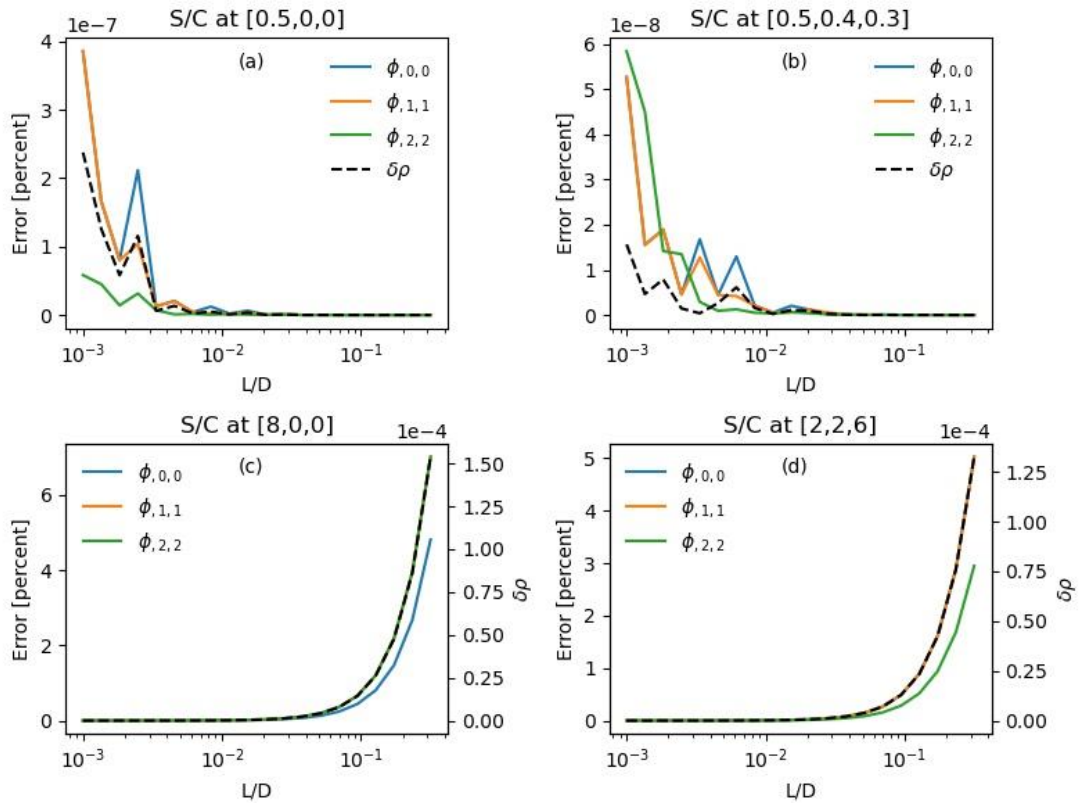
332

333 The eight-probe scheme will now be examined for the electric field produced by a
 334 uniformly-charged ball.

335 The relationship between the relative truncation errors and the relative
 336 measurement scale, L/D , is studied when we set $L_x = L_y = L_z = l_z$ and scale up and
 337 down the distances between the spacecraft to adjust L/D . Due to the broken spherical
 338 symmetry, two points inside the ball, $[0.5,0,0]$ and $[0.5,0.4,0.3]$, and two points
 339 outside of the ball, $[8,0,0]$ and $[2,2,6]$, are chosen as the representative points. The
 340 modeled results are shown in Fig. 10. The quadratic gradient in the ball is close to a
 341 constant and the charge density here is a constant. The truncation errors given by the
 342 algorithm, as shown in Fig. 10 (a,b), are negligible in this case. The charge density
 343 outside the ball is zero, and the calculated density, amounting to 10^{-4} as shown by the
 344 dashed lines in Fig 10 (c,d), is fairly close to zero. Note that the scale is one in the
 345 modeled system. As $L/D < 0.1$, the truncation errors of the quadratic gradient are less

346 than 2%. It can be seen that the relative errors of the quadratic gradient and hence the
 347 charge density are at second order in L/D .

348



349

350 **Figure 10.** Panel (a) and (b) show the relative truncation errors of the quadratic gradient
 351 of the electric potential (solid lines) and the charge density (dashed lines) at $[0.5,0,0]$
 352 and $[0.5,0.4,0.3]$ in the ball, respectively. Panel (c) and (d) show the relative
 353 truncation errors of the quadratic gradient of the electric potential (solid lines and left
 354 vertical axis) and the absolute errors of the charge density (dashed lines and right
 355 vertical axis).

356

357 For real measurements in space, the distances between the probes along the z-axis,
 358 L_z and l_z , are much smaller than those along the other axes, L_x and L_y .

359 This 8 probe scheme is potentially applied for the net charge measurements on the
360 high altitude orbits, for which the spacecraft is spinning thus that the four probes can
361 stretch out at the ends of the four wire booms on the spin plane as shown in Fig. 9.

362

363 **5. Summary and Discussions**

364 Preliminary explorations for measuring the net charge density in space have been
365 presented in this paper. Three schemes for the charge density measurements have been
366 developed.

367 The first scheme deduces the charge density based on four spacecraft electric field
368 measurements. Based on the electric fields (\mathbf{E}_α , $\alpha = 1,2,3,4$) observed at the four
369 spacecraft, we can obtain the gradient of the electric field at the barycenter of the
370 constellation, $(\nabla\mathbf{E})_c$, and furthermore, the divergence of the electric field, $(\nabla \cdot \mathbf{E})_c$.
371 The Gaussian theorem yields the charge density as $\rho = \epsilon\nabla \cdot \mathbf{E}$. This algorithm requires
372 the constellation not to be distributed in a plane or linearly. In other words, the three
373 eigenvalues of the volumetric tensor of the constellation should be non-vanishing.
374 Based on this algorithm, an analysis on the electric field data acquired during a dayside
375 magnetopause crossing event by the MMS constellation shows a charge separation in
376 the magnetopause boundary layer and that the positive charges are accumulated on the
377 magnetospheric side while the negative charges are accumulated on the magnetosheath
378 side. A normal electric field pointing at the magnetosheath is also discovered. This
379 confirms a previous theoretical prediction (Parks, 1991; Kivelson and Russell, 1995).

380

381 Another charge density measurement scheme is based on 10 or more electric
382 potential probes. By using a newly-developed algorithm [Shen et al., 2021], the linear
383 gradient, $(\nabla\phi)_c$, and the quadratic gradient, $(\nabla\nabla\phi)_c$, of the electric potential at the
384 center of the probes can be calculated from the $N \geq 10$ electric potentials,
385 $\phi_\alpha (\alpha = 1, 2, \dots, N)$, as measured at the N probes. Furthermore, the electric field and
386 the net charge density at the center of the probes can be calculated using $\mathbf{E} = -(\nabla\phi)_c$
387 and the Poisson equation, $\rho = -\epsilon\nabla^2\phi$, respectively.

388 This scheme requires the probes to be distributed uniformly. In other words, the
389 eigenvalues of the 6×6 matrix \mathfrak{R} should be non-vanishing. The accuracy of the
390 charge density estimated by the algorithm is of first order and that of the electric field
391 is of second order. Modeling also shows that more probes lead to higher accuracy.

392

393 Finally, two other schemes are presented to measure the electric charge density,
394 which improve on the existing schemes for electric field observations onboard
395 spacecraft. If one more electric potential probe is added in addition to the six electric
396 potential probes of the electric field equipment on board the MMS spacecraft (that are
397 distributed symmetrically on the three axes of the Cartesian coordinate system), the
398 charge density can be derived along with the electric field vectors. The seventh probe
399 is placed at the origin of the coordinate system. Due to the shielding potential of the
400 spacecraft, this seven-probe scheme cannot be applied to measurements in space.
401 However, it can be utilized in charge density measurements in ground-based laboratory
402 experiments. Alternatively, by placing two more probes symmetrically on the two stiff

403 booms in the six-point scheme of the MMS constellation, the eight-probe scheme will
404 work for charge density measurements in space. The simulation test shows that the
405 estimated electric field is of fourth-order accuracy and the charge density is of second-
406 order accuracy. The truncation errors contained in this scheme are much less than those
407 in the 10 -probe scheme. The implementation of this scheme requires further
408 development in the future.

409

410

411

412

413

414

415

416

417

418

419

420

421

422

423

424

425

426 **Acknowledgments**

427 This work was supported by National Natural Science Foundation (NSFC) of China
428 (Grant No. 41874190) and the Shenzhen Technology Project
429 (JCYJ20190806144013077). The MMS data were obtained from the MMS Science
430 Data Center (<http://lasp.colorado.edu/mms/sdc/>). We thank the MMS plasmas and
431 field teams for providing with these high quality data.

432

433

434

435

436

437

438

439

440

441

442

443

444

445

446

447

448 **References**

449 Akasofu, S.-I. (1981), The aurora: An electrical discharge phenomenon surrounding the
450 Earth. *Rep. Prog. Phys.*, 44, 1123.

451 H Alfvén. (1963), *Cosmical Electrodynamics: Fundamental Principles*, by Hannes
452 *Alfvén and Carl-Gunne Fälthammar.*, p. 158-159, Clarendon Press.

453 Axford, W. I. (1968). The polar wind and the terrestrial helium budget. *J. Geophys. Res.*,
454 73, 6855.

455 Berthelier, J. J., M. Godefroy, F. Leblanc, M. Malingre, M. Menvielle, et al. (2005),
456 ICE, the electric field experiment on DEMETER. *Planetary and Space Science*,
457 54(5), 456–471. <https://doi.org/10.1016/j.pss.2005.10.016>

458 Bittencourt, J. A. (2004), *Fundamentals of plasma physics*, p. 256. Springer.

459 Block, L. (1975), Double layers, in *Physics of the Hot Plasma in the Magnetosphere*,
460 edited by B. Hultqvist and L. Stenflo, p. 229, Springer, New York.

461 Burch, J. L., Moore, T. E., Torbert, R. B., and Giles, B. L. (2016), Magnetospheric
462 Multiscale overview and science objectives. *Space Science Reviews*, 199(1-4), 5–
463 21. <https://doi.org/10.1007/s11214-015-0164-9>.

464 Chanteur, G. (1998), Spatial Interpolation for four spacecraft: Theory, in *Analysis*
465 *Methods for Multi-Spacecraft Data*, edited by G. Paschmann and P. W. Daly, p. 349,
466 ESA Publ. Div., Noordwijk, Netherlands.

467 Harvey, C. C. (1998), Spatial gradients and the volumetric tensor, in *Analysis Methods*
468 *for Multi-Spacecraft Data*, edited by G. Paschmann and P. W. Daly, p. 307, ESA

469 Publications Division, Noordwijk, The Netherlands.

470 Hasegawa, A. and I. Sato (1989), *Space Plasma Physics, I Stationary Processes*, p. 153-
471 156, Springer-Verlag, Berlin, Heidelberg, Germany.

472 Lemaire, J., and V. Pierrard (2001), Kinetic Models of Solar and Polar Winds.
473 *Astrophysics and Space Science*, 277, 169–180.

474 Michael, C. K. (2014), *The Earth's Electric Field: Sources From Sun to Mud*, p. 66, 168,
475 204, Elsevier, 225 Wyman Street, Waltham, MA 02451, USA.

476 Mozer F. S., and Bruston, P. (1967), Motion of artificial ion clouds in upper atmosphere.
477 *Journal of Geophysical Research*, 72, 1109-1114.

478 Mozer, F. S. (1973), Analyses of techniques for measuring dc and ac electric fields in
479 the magnetosphere. *Space Sci. Rev.*, 14, 272-313.

480 Parks, G. K. (1991), *Physics Of Space Plasmas: An Introduction*, p. 355-369, Redwood
481 City, CA, Addison-Wesley Publishing Co..

482 Paschmann G., F. Melzner, R. Frenzel, et al. (1997), The electron drift instrument for
483 Cluster[J]. *Space Science Reviews*, 79, 233-269.

484 Pedersen A. F., Mozer F. S., and Gustafsson G. (1998), Electric field measurements in a
485 tenuous plasma with spherical double probes, in *Measurement Techniques in Space*
486 *Plasmas – Fields*, edited by R. F. Pfaff, J. E. Borovsky, and D. T. Young, p. 1-12,
487 AGU Geophysical Monograph 103, AGU, Washington DC.

488 Pollock, C., Moore, T. E., Jacques, A., Burch, J., Gliese, U., Saito, Y., et al. (2016), Fast
489 plasma investigation for Magnetospheric Multiscale. *Space Science Reviews*,
490 199(1-4), 331–406. <https://doi.org/10.1007/s11214-016-0245-4>.

491 Raadu, M. A. (1989), The physics of double layers and their role in astrophysics. Phys.
492 Rep., 178, 25.

493 Robert, P., et al. (1998), Tetrahedron geometric factors, in *Analysis Methods for Multi-*
494 *Spacecraft Data*, edited by G. Paschmann and P. W. Daly, p. 323, ESA Publications
495 Division, Noordwijk, The Netherlands.

496 Shen, C., X. Li, M. Dunlop, Z. X. Liu, A. Balogh, D. N. Baker, M. Hapgood, and X.
497 Wang (2003), Analyses on the geometrical structure of magnetic field in the current
498 sheet based on cluster measurements, *J. Geophys. Res.*, 108(A5), 1168,
499 doi:10.1029/2002JA009612.

500 Shen, C., Dunlop, M., Li, X., Liu, Z. X., Balogh, A., Zhang, T. L., Carr, C. M., Shi, Q.
501 Q., and Chen, Z. Q. (2007), New approach for determining the normal of the bow
502 shock based on Cluster four-point magnetic field measurements, *J. Geophys. Res.*,
503 112, A03201, doi:10.1029/2006JA011699.

504 Shen, C., Zhou, Y. F., Ma, Y. H., Wang, X. G., Pu, Z. Y., Dunlop, M. (2021), A general
505 algorithm for the linear and quadratic gradients of physical quantities based on 10 or
506 more point measurements, *J. Geophys. Res.*, in submission.

507 Torbert, R. B., Russell, C. T., Magnes, W., Ergun, R. E., Lindqvist, P.-A., LeContel, O.,
508 et al. (2016), The FIELDS Instrument Suite on MMS: Scientific objectives,
509 measurements, and data products. *Space Science Reviews*, 199, 105–135.
510 <https://doi.org/10.1007/s11214-014-0109-8>

511 Treumann, R. A., and Baumjohann, W. (1997). *Advanced Space Plasma Physics*. p. 31-
512 33, 155-167. Imperial College Press, 516 Sherfield Building, Imperial College,

513 London.

514 Yau, A. W., Takumi, A., and Peterson, W. K. (2007). The polar wind: Recent
515 observations[J]. Journal of Atmospheric and Solar-Terrestrial Physics, 69, 1936-
516 1983.

517

518

519

520

521

522

523

524

525

526

527

528

529

530

531

532

533

534

535

536 **Figure Captions**

537

538 **Figure 1.** A schematic view of the measurements of the electric field by the MMS
539 constellation and the calculation of the charge density.

540

541 **Figure 2.** The structure of the magnetopause during an MMS crossing event on 9
542 January 2017. From top to bottom: (a) the magnetic flux density at the center of the
543 constellation, (b) the electron and ion number densities measured by MMS-1 (Pollock
544 et al., 2016), (c) the rotation rates of the magnetic field (Shen et al., 2007), (d) $|\nabla|\mathbf{B}||$,
545 (e) the radius of curvature of the magnetic field lines (Shen et al., 2003), and (f) the
546 charge distribution. The yellow shading indicates the rotational discontinuity (RD)
547 crossing.

548

549 **Figure 3.** The distribution of the 10 probes.

550

551 **Figure 4.** The relative errors of the linear (a) and the quadratic (b) electric potential
552 gradients, i.e., $\partial_x\phi$ and $\partial_x\partial_x\phi$, calculated for different numbers of iterations at
553 $[0.1,0,0]$ within the charged ball.

554

555 **Figure 5.** The left panels, (a), (b), and (c), show the truncation errors for the non-
556 vanishing component of the linear gradient by L/D calculated for three different

557 locations of the barycenter of the 10 probes inside the ball, $[0.1,0,0]$, $[0.4,0,0]$, and
558 $[0.7,0,0]$. The right panels, (b), (d), and (f), illustrate the relative errors of the non-
559 vanishing components of the quadratic gradient and charge density (dashed line)
560 calculated for the same three locations of the barycenter. It is noted that $\phi_{,1} \equiv \partial_x \phi$
561 and $\phi_{,2,2} \equiv \partial_y \partial_y \phi$, where a comma denotes partial differentiation.

562

563 **Figure 6.** The left panels, (a), (b), and (c), show the truncation error for the non-
564 vanishing component of the linear gradient as a function of L/D calculated for three
565 different locations of the barycenter of the 10 probes outside of the ball, $[3,0,0]$,
566 $[5,0,0]$, and $[8,0,0]$. The right panels, (b), (d), and (f), illustrate the relative errors of
567 the non-vanishing components of the quadratic gradient and the absolute value of the
568 charge density (dashed line) calculated for the same three locations of the barycenter. It
569 is noted that the real charge density outside of the ball is zero.

570

571 **Figure 7.** The relation between the absolute error of the charge density and the number
572 of measurement points at $[3,0,0]$. The relative measurement scale is chosen as $L/D =$
573 0.05 (left) and $L/D = 0.01$ (right). The dashed lines are fitted from the modeled
574 errors.

575

576 **Figure 8.** A schematic view of the seven-probe measurement of the charge density. The
577 probes are indicated by black dots.

578

579 **Figure 9.** A schematic view of the eight-probe measurement of charge density.

580

581 **Figure 10.** Panel (a) and (b) show the relative truncation errors of the quadratic gradient
582 of the electric potential (solid lines) and the charge density (dashed lines) at $[0.5,0,0]$
583 and $[0.5,0.4,0.3]$ in the ball, respectively. Panel (c) and (d) show the relative
584 truncation errors of the quadratic gradient of the electric potential (solid lines and left
585 vertical axis) and the absolute errors of the charge density (dashed lines and right
586 vertical axis).

587